A detailed analysis of the energy levels configuration existing in the band gap of supersaturated silicon with titanium for photovoltaic applications

E. Pérez, S. Dueñas, H. Castán, H. García, L. Bailón, D. Montero, R. García-Hernansanz, E. García-Hemme, J. Olea, and G. González-Díaz

The energy levels created in supersaturated n-type silicon substrates with titanium implantation in the attempt to create an intermediate band in their band-gap are studied in detail. Two titanium ion implantation doses (10^{13} cm^{-2} and 10^{14} cm^{-2}) are studied in this work by conductance transient technique and admittance spectroscopy. Conductance transients have been measured at temperatures of around 100 K. The particular shape of these transients is due to the formation of energy barriers in the conduction band, as a consequence of the band-gap narrowing induced by the high titanium concentration. Moreover, stationary admittance spectroscopy results suggest the existence of different energy level configuration, depending on the local titanium concentration. A continuum energy level band is formed when titanium concentration is over the Mott limit. On the other hand, when titanium concentration is lower than the Mott limit, but much higher than the donor impurity density, a quasi-continuum energy level distribution appears. Finally, a single deep center appears for low titanium concentration. At the n-type substrate, the experimental results obtained by means of thermal admittance spectroscopy at high reverse bias reveal the presence of single levels located at around E_c-425 and E_c-275 meV for implantation doses of 10^{13} cm^{-2} and 10^{14} cm^{-2}, respectively. At low reverse bias voltage, quasi-continuously distributed energy levels between the minimum of the conduction bands, E_c and E_c-450 meV, are obtained for both doses. Conductance transients detected at low temperatures reveal that the high impurity concentration induces a band gap narrowing which leads to the formation of a barrier in the conduction band. Besides, the relationship between the activation energy and the capture cross section values of all the energy levels fits very well to the Meyer-Neldel rule. As it is known, the Meyer-Neldel rule typically appears in processes involving multiple excitations, like carrier capture and emission in deep levels, and it is generally observed in disordered systems. The obtained Meyer-Neldel energy value, 15.19 meV, is very close to the value obtained in multicrystalline silicon samples contaminated with iron (13.65 meV), meaning that this energy value could be associated to the phonons energy in this kind of substrates.

I. INTRODUCTION

The formation of an intermediate band (IB) in the mid gap of semiconductors has been widely studied in the last decade because of its potentiality of improving the efficiency of single junction solar cells.[1] This approach would enable electrons to be pumped from the valence band to the conduction band via two-photon absorption of photons with lower energy than the semiconductor band gap.[2] Consequently, single junction solar cells based on semiconductors with an IB could reach efficiency values above the maximum theoretical efficiency for single junction cells established by Shockley and Queisser in 40.7%.[1,3] IB solar cells could reach an efficiency value up to 63.1%,[1] better than the theoretical maximum for two-junction solar cells (55.9%).[4] Another advantage of IB semiconductors is the capability to detect infrared radiation by silicon-based devices through the absorption of photons with energies below its band gap.[5,6]

There are several ways to form the IB in a semiconductor: by means of quantum dots in the semiconductor,[7] or by using highly mismatched alloys like GaNAsP,[8] ZnTeO,[9] and GaInNAs.[10] Other options include the implantation of semiconductor substrates like Cu_2O with high doses of dopants like N,[11] or the implantation of silicon substrates with very high doses of transition metals, Ti atoms, for instance.[12,13]

Titanium is a well-known impurity in silicon. According to the literature, Ti can introduce up to four different deep levels in the silicon band gap depending on its atomic configuration in the silicon grid.[14] The first one is an acceptor level located between E_c–0.06 and E_c–0.09 eV.[14,15] The second one is a donor level located between E_c–0.3 and E_c–0.21 eV,[14,17] which could behave as a shallow dopant. The third one is a donor level located between $E_v + 0.25$ and E_v+0.33 eV.[14,17] Finally, there is a level between E_c–0.51 and E_c–0.55 eV,[16,17] the most unknown of the four levels. Although these impurities are a well-known source of non-radiative Shockley-Read-Hall (SRH) recombination,[18,19] it has been argued that

this recombination may be suppressed if the Ti concentration is high enough to exceed the Mott limit (5.9×10^{19} cm^{-3}).[2,20] At these concentrations, a continuous energy band is theoretically formed, the IB, instead of several single-energy levels.

In this context, the goal of the present study is to carry out a deeper study of the energy levels detected in silicon substrates implanted with high concentrations of titanium, just under the Mott limit, reported in a previous work.[21] In order to obtain some knowledge about the configuration of these energy levels, Thermal Admittance Spectroscopy (TAS) and Conductance Transient (GTT) techniques were applied.

II. EXPERIMENTAL SETUP

300 μm Si (111) n-type samples ($\mu = 1450\,\text{cm}^2/\text{V s}$; $n = 2.2 \times 10^{13}$ cm^{-3} at room temperature) were implanted in an ion beam service (IBS) refurbished VARIAN CF3000 Ion Implanter at 32 KeV with Ti at high doses: 10^{13} and $10^{14}\,\text{cm}^{-2}$. In both cases, the concentration profiles are below the Mott limit at any depth.[22]

Bottom and top electrodes were fabricated by aluminum evaporation. To obtain good ohmic contacts on the bottom, n^+ layer were fabricated on the back side of the samples (substrate) by ion implantation of phosphorous in a dose of $10^{15}\,\text{cm}^{-2}$ at energy of 80 keV. Afterwards, samples were annealed at 900 °C during 20 s. Then, the implanted Si samples were annealed by means of the pulsed laser melting (PLM) method to recover the crystal lattice.[23] The combination of two highly non-equilibrium techniques (ion implantation and subsequent PLM treatment) allows to build up a new class of semiconductors that avoid equilibrium constraints. The PLM annealing process was performed by IPG Photonics (New Hampshire, USA). Samples were annealed with one 20 ns long pulse of a KrF excimer laser (248 nm) at energy density of 0.8 J/cm^2. PLM is a highly non-equilibrium processing technique which is able to melt and recrystallize the Si surface up to about 100 nm deep in very short times (10^{-8}–10^{-6} s). This rapid re-crystallization time allows the incorporation of Ti atoms to the Si at concentrations well above the solubility limit for this element.[12,13,16] Moreover, the PLM processing of the Ti implanted Si layer prevents secondary phase formation (i.e., Ti silicide) even when the equilibrium solubility limit has been greatly exceeded.

Depth profiles of Ti atoms in the Si lattice were obtained by time-of-flight secondary ion mass spectrometry (ToF-SIMS) characterization. These were carried out with a TOFSIMS IV model manufactured by ION-TOF, using a 25 keV pulsed Bi^{3+} beam at 45° incidence. The secondary ions generated were extracted with a 10 keV voltage, and their time of flight from the sample to the detector was measured in a reflection mass spectrometer. Figure 1 shows the Ti depth profiles or implanted samples at 10^{13}, 10^{14}, 10^{15}, and $10^{16}\,\text{cm}^{-2}$ both as deposited and after a PLM process at 0.8 J/cm^2. As comparison we have plotted also the profiles for the non-annealed samples. As it can be seen, Ti profiles have been pushed to the Si surface, becoming steeper and with a higher and sharp maximum although this effect is more

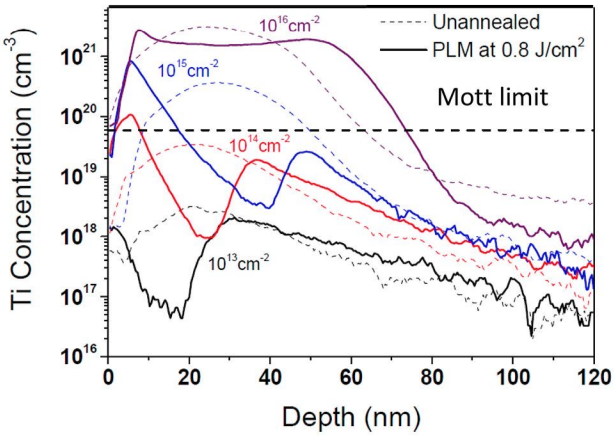

FIG. 1. ToF-SIMS profiles of Ti-implanted samples with 10^{13}, 10^{14}, 10^{15}, and $10^{16}\,\text{cm}^{-2}$ nonannealed (dashed) and after PLM annealing at 0.8 J/cm^2 (solid).

pronounced for lower doses. The second peak that appears clearly for 10^{13}, 10^{14}, and $10^{15}\,\text{cm}^{-2}$ doses at 30, 40, and 50 nm, respectively, marks the border between melted and unmelted semiconductor zone. Clearly, the melted deep is related with the degree of amorphization which in turn is directly dependent on the implanted dose.

Top contacts consist of 1 cm^2 square electrodes fabricated by aluminum evaporation. These contacts resulted to be ohmic for samples over the Mott limit. For samples under the Mott limit, the contacts are ohmic at temperatures over 70 K and become partially rectifier for very low temperatures, probably due to that titanium impurities are not totally ionized. This experimental evidence allows us to neglect the effect of the top electrode in the experimental results presented in this work, which have been obtained at temperatures over liquid nitrogen temperature (77 K).

The TAS technique yields thermal emission rates (e^t) of deep levels by measuring the variations of capacitance and conductance of a junction as a function of temperature and frequency.[24–26] These variations are due to thermally induced changes of the trap emission and capture time rates with respect to the frequency of the measuring signal. Experimental measurements consist on recording the conductance and capacitance while keeping constant the frequency of the measuring signal and varying the temperature. Each trap existing in the junction shows a maximum in conductance (G_m) at a temperature T_m and an inflection point in capacitance (C_i) at a temperature T_i, from which we can obtain its thermal emission rate, according the following equations:[25]

$$e^t(T_m) = \frac{\omega}{1.98}, \tag{1}$$

$$e^t(T_i) = \frac{\omega}{1.825}. \tag{2}$$

The emission and capture process occur at the point in the space charge region where the occupation factor of the trap is of about 1/2. By measuring at different frequencies, the thermal dependency of e^t is obtained, from which the activation energy (E_T) and the capture cross section (σ_T) can be derived.

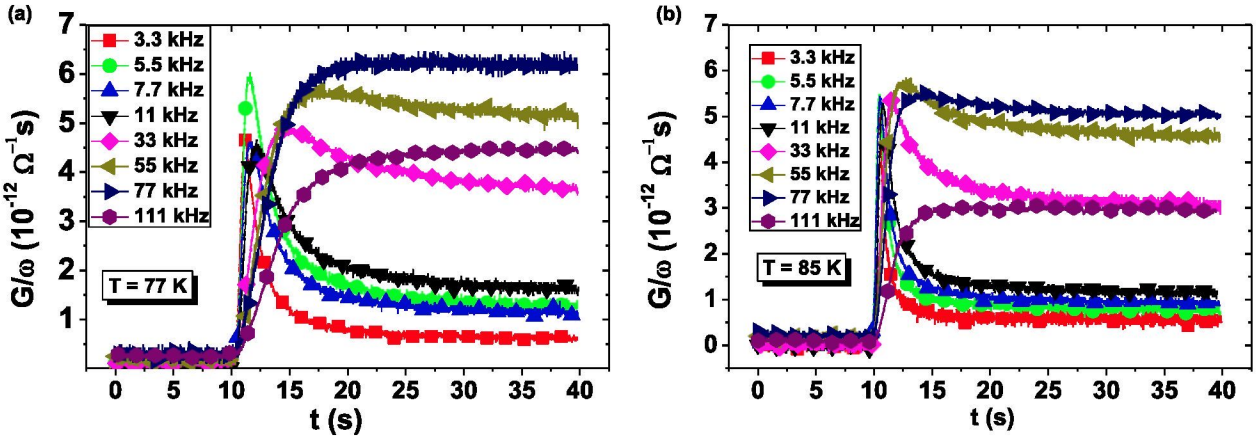

FIG. 2. Conductance transients corresponding to $10^{14}\,cm^{-2}$ implantation dose at 77 K (a) and 85 K (b).

Admittance was measured by using an EG&G 5210 lock-in amplifier, and a Femto DLPCA-200 current preamplifier. A Keithley 617 Electrometer applied DC bias and an HP33120A signal generator were used to apply small ac signals. Samples were cooled on an Oxford Instruments Spectrostat DN cryostat, and an Oxford Instruments ITC502 controller was used to measure and control the temperature.

On the other hand, GTT technique provides the border trap density of MIS structures as a function of the energy and the spatial position.[27,28] This capability is used here to study supersaturated silicon substrates. The variation with the frequency and temperature of the conductance transients caused by the bias pulses gives information about the energy levels distribution in the band gap. Experimental setup was the same as for TAS plus an HP81104A pulse generator and an HP-54501A digital oscilloscope to record the conductance transients.

III. EXPERIMENTAL RESULTS

In this section, we describe the experimental results obtained when measuring conductance of the samples in both transient (GTT) and steady-state (TAS) regimes.

The shape of conductance transients strongly depends on the frequency of the ac signal and temperature. At temperatures below 105 K, transients show different behavior for low and high frequencies. GTT measurements corresponding to samples with an implantation dose of $10^{14}\,cm^{-2}$ are shown in Fig. 2. Transients are obtained by measuring the conductance signal at a given frequency when samples are submitted to a dc bias pulse. The bias pulse consists on applying a negative voltage of −2 V during 10 s, followed by 0.2 V during 30 s. The frequency of the ac signal was varied from 3.3 to 120 kHz.

At low frequency values, we observe that conductance transients first increase and then decrease asymptotically reaching a stationary value. At higher frequencies, conductance increases up to a stationary value. At temperatures over 105 K, conductance transients are similar to those appearing at low frequencies in Fig. 2. Similar behavior is observed in samples implanted with $10^{13}\,cm^{-2}$ dose, but at lower temperatures (below 90 K). As we will discuss later, the shape of these transients can be explained taking into account that the high impurity concentration induces a band gap narrowing[29] on the IB layer. In consequence, a barrier energy for electrons appears which acts as a blocking layer at low temperatures. Experimental evidences of the existence of this blocking layer have been also published elsewhere.[30]

Steady-state conductance as a function of temperature and frequency was obtained by TAS technique. The most noticeable result in this work is that the number and position of conductance peaks vary with the bias voltage. Some examples are plotted in Figs. 3–5. Two deep levels were detected at −1 V bias value, as shown in Fig. 3 for the sample with $10^{14}\,cm^{-2}$ implanted dose.

The activation energies of these levels were obtained from the corresponding Arrhenius plot showed in the inset. In the same way, two deep levels were also detected at −3 V bias value, as Fig. 4 shows for the sample with $10^{13}\,cm^{-2}$ implanted dose. In contrast, for reverse bias values higher than 3 V, only one deep level is present in each conductance curve, as it is shown in Fig. 5 for the sample with $10^{14}\,cm^{-2}$ implanted dose. It is important to point out that the measured energy values increase with reverse bias voltage. On the other hand, in these figures, we can also observe that conductance

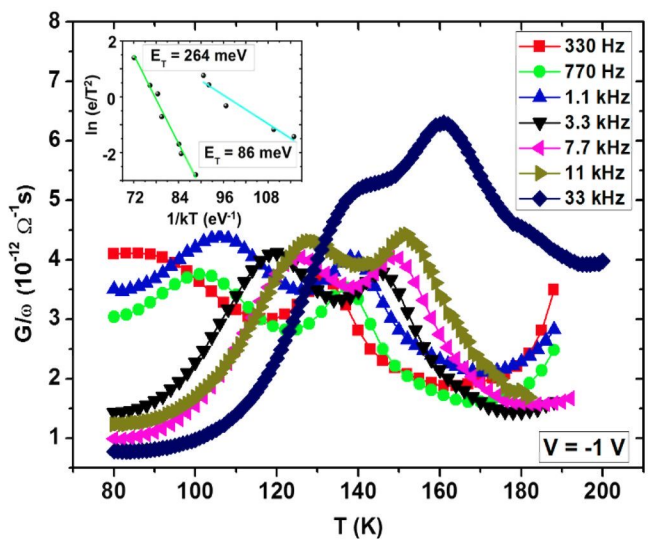

FIG. 3. G/ω-T curves and the Arrhenius plot corresponding to $10^{14}\,cm^{-2}$ implantation dose. The bias voltage value is −1 V.

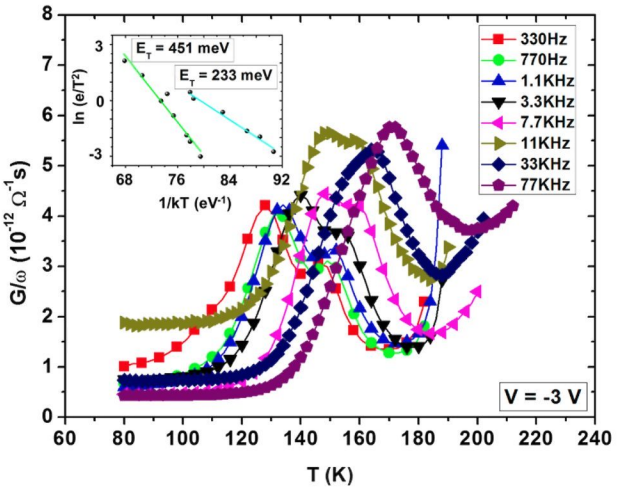

FIG. 4. G/ω-T curves and the Arrhenius plot corresponding to $10^{13}\,cm^{-2}$ implantation dose. The bias voltage value is -3 V.

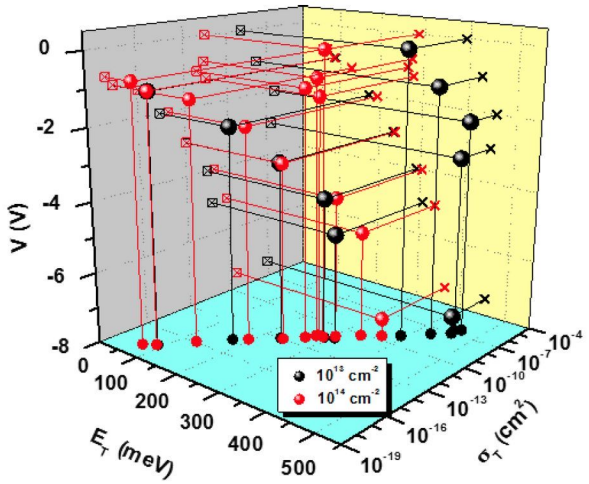

FIG. 6. Plot representing together activation energy, capture cross section, and voltage bias values for each energy level detected in samples with Ti concentrations under the Mott limit. E_T represents the energy value below E_C. Projections on the three planes are marked to improve the readability.

peaks become narrower as reverse voltage increases. These facts are due to the existence of multiple energy levels as we will discuss in Sec. IV.

In Figure 6, we summarize all deep levels measured by TAS. In this figure, we plot together the activation energy and capture cross section, σ_T, and the voltage bias at which each energy level was detected. A thorough examination of all levels detected with TAS reveals a dependency among capture cross section and activation energy for all deep levels detected.[21] To facilitate this analysis, the two-dimensional projections that involve the voltage magnitude are used instead of the three-dimensional plot. Figure 7(a) shows the activation energy values versus the bias voltage values, and Figure 7(b) shows the capture cross section values versus the bias voltage values.

Focusing in the activation energy values (Fig. 7(a)), we see that there is one single level and also some quasi-continuously distributed levels for both values of implantation dose. In the samples with $10^{13}\,cm^{-2}$ implantation dose, the single level appears for bias values between -3 V and 0 V with an energy value between 391 and 460 meV below E_C (region A). As Fig. 3 shows, this level corresponds to the higher temperature conductance peaks when two peaks in each conductance curve are found. In the samples with $10^{14}\,cm^{-2}$ implantation dose, this single level appears for bias values between -1.25 and 0 V with an energy value between 264 and 287 meV below E_C (region B). For all voltage bias, additional peaks appear with energies continuously increasing from 450 meV below E_C to almost E_C (region C). These levels correspond to the lower temperature conductance peaks in Figs. 3 and 4, where two peaks appear, and to the only one appearing at higher voltage bias, as Fig. 5 shows.

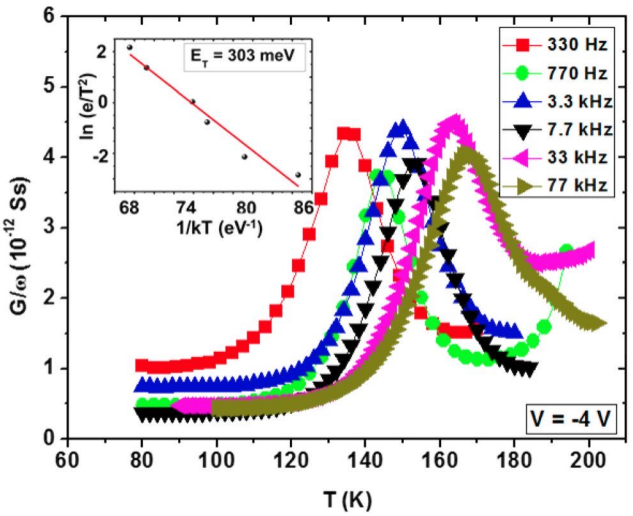

FIG. 5. G/ω-T curves and the Arrhenius plot corresponding to $10^{14}\,cm^{-2}$ implantation dose. The bias voltage value is -4 V.

IV. DISCUSSION

Based on the experimental results described in Sec. III, an energy-level-configuration model for Ti impurities on silicon is proposed (see Fig. 8). To understand this model, we have to keep in mind that the implantation profile strongly vanishes from the high impurity concentration region up to the non-implanted substrate where there is only a small Ti concentration at locations close to the implanted region. The two main concepts in which our model is based are direct consequence of the high Ti concentration: (i) energy level splitting (ELS), and (ii) band gap narrowing (BGN).

In Fig. 8(a), we differentiate three different energy level configurations, depending on the Ti concentration. As it has been established elsewhere,[30] when Ti concentration is over the Mott limit ($5.9 \times 10^{19}\ cm^{-3}$), an IB, consisting on a continuous energy level distribution, is formed. On the other hand, when Ti concentration is low, impurities create single deep levels. Finally, an intermediate situation appears when Ti concentration is very high but still lower than the Mott limit: traps are so close that interaction between them induces the energy levels splitting and a quasi-continuum energy band appears (QC-region). In previous works,[30] it has been demonstrated the formation of the intermediate band on samples with Ti concentration over the Mott limit. In this work,

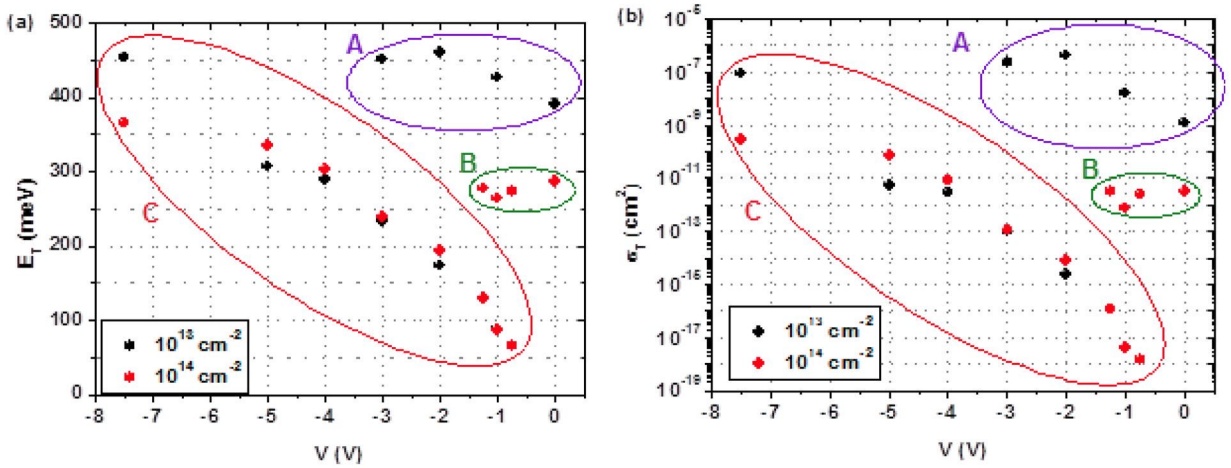

FIG. 7. Plot of the activation energy (a) and capture cross section (b) values versus bias voltage values.

the samples do not reach the Mott limit at any location (see Fig. 1), but Ti concentration is high enough to induce multiple energy levels in the implanted region. That is the reason why in Figs. 8(b) and 8(c) we distinguish two regions in our samples: the QC-region, where the Ti concentration is very high, and the single deep level configuration at locations of the implantation profile tail where the Ti concentration is low. The transition between both regions is gradual, and a boundary between them cannot be established.

On the other hand, it has been experimentally demonstrated that a shrinkage of the band-gap appears when the impurity concentration is high. The BGN effect is ascribed to the emerging of the impurity band formed by the overlapped impurity states. The shifts in the band edges represent a potential barrier which influences the carrier transport across the junctions.[29] The above considerations allow us to draw the band diagrams plotted in Figs. 8(b) and 8(c) corresponding to zero and negative bias condition. As the Ti concentration gradually decreases from the implanted layer to the bulk region, the BGN yields to a gradual increase of the conduction band as it is plotted in Fig. 8(b). And when applying a reverse voltage bias, the conduction band is modified in accordance with Fig. 8(c). Several models have been proposed to calculate the band gap narrowing, ΔE_g^{bgn}, between bands. In 1991, Jain and Roulston proposed a simple expression for BGN in heavily doped semiconductors.[31] This model provides values of 25 and 55 meV for doping concentrations of 10^{18} and $10^{19}\,\mathrm{cm}^{-3}$, respectively. A more accuracy model was proposed by Palankovsky *et al.*[32] in 1999. In this model, the effect of the temperature is also included, yielding BGN values at low temperatures of about 50 meV for $10^{18}\,\mathrm{cm}^{-3}$ and 130 meV for $10^{19}\,\mathrm{cm}^{-3}$. Assuming that the BGN equally affects to the conduction and valence band, we can estimate values for the conduction band shrinkage as $\Delta E_{cB}^{bgn} = \Delta E_g^{bgn}/2$. We use the values of ΔE_{cB}^{bgn} at low temperatures as the energy barrier plotted in Fig. 8. In Fig. 1, we observe that samples implanted with $10^{13}\,\mathrm{cm}^{-2}$ dose reach maximum Ti concentrations of $2 \times 10^{18}\ \mathrm{cm}^{-3}$ which corresponds to a conduction band lowering, ΔE_{cB}^{bgn}, of about 30 meV. In the case of samples implanted with $10^{14}\,\mathrm{cm}^{-2}$ dose, maximum Ti concentration is of $3 \times 10^{19}\ \mathrm{cm}^{-3}$ which yield a conduction band lowering of slightly higher than 60 meV. These values are several times higher than kT (equal to 8.5 meV at 100 K) and, then, the effect of the so formed energy barrier cannot be neglected. Profiles plotted in Fig. 1 can be used to calculate the band-gap narrowing as a function of the distance from the sample surface. In Figure 9, we have used the Palankovsky *et al.*[32] model to obtain an accurate ΔE_{cB}^{bgn} profile in which we observe how the fluctuations on the Ti profile affect to the conduction band narrowing.

Now, the experimental results described in Section III can be explained. In Fig. 2, we see that conductance transients appear when a reverse to zero or positive bias is applied. Conductance first increases and afterwards falls to a stationary value which depends on the frequency. At reverse bias, current and conductance of the junction are zero due to the above explained conduction band barrier. When bias is changed to zero or positive values, the space charge region shrinks, and electrons and holes are injected to the quasi-neutral regions of the space charge region yielding to a current transient from low (reverse) current to the stationary forward current. The forward current is due to electrons injected from the n-type substrate to the highly doped layer. At low temperatures, electrons are at the minimum of the conduction band. When voltage changes from reverse to forward values, carriers have to traverse the energy barrier by tunneling (see Fig. 8(b)). Since tunneling is time consuming, it induces a time delay between voltage and current which depends on the barrier height and thickness. In Fig. 2, we can see that the time delays are in the range of several seconds and decrease as temperature increases. For samples implanted at lower doses ($10^{13}\,\mathrm{cm}^{-2}$), as the barrier is lower and thinner this effect occurs at lower temperatures and delay times are lower as well. The time delay between voltage and current induces a loss term which yields to a conductance signal which increases at the beginning and decays up to a stationary value for long times. This stationary value depends on the ratio between the delay time constant and the ac frequency signal. For low frequencies, the ac signal period is much higher than the tunneling time constant and, then, electrons have enough time to go and back through the barrier and their response has not loss (conductance) term. At high frequency, signal changes cannot be

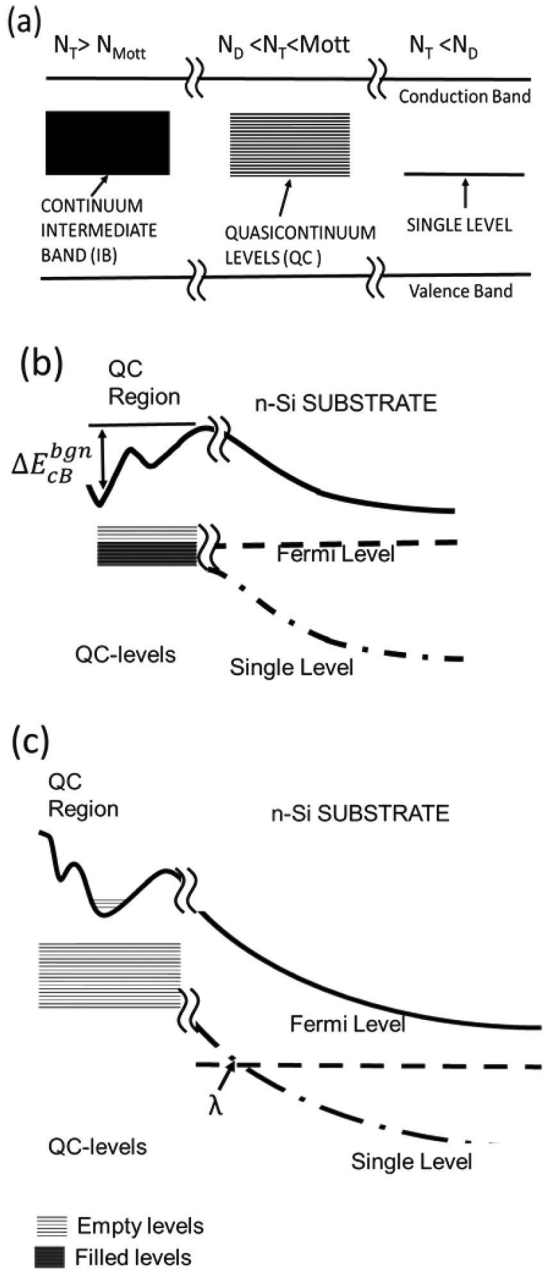

FIG. 8. Energy level configuration (a), and band diagram at zero (b) and reverse (c) bias voltage of a supersaturated sample.

followed by tunneling carriers and, so, the loss term and, i.e., the conductance, increase with frequency. As temperature increases, the ΔE_{cB}^{bgn} value decreases[32] and, at the same time, electrons gain energy transferred from the semiconductor lattice phonons (proportional to kT). These two additive contributions make easier for electrons to overcome the energy barrier. In consequence, the time delay between voltage and current trends to zero and not conductance transient neither stationary conductance signal are observed at temperatures higher than around 110 K.

Although a detailed calculation of the tunneling emission rate between the traps and the conduction band is complex and out of the scope of this work, an estimation of the temperature range where tunneling rate prevails over thermal emission rate can be roughly made as follows.

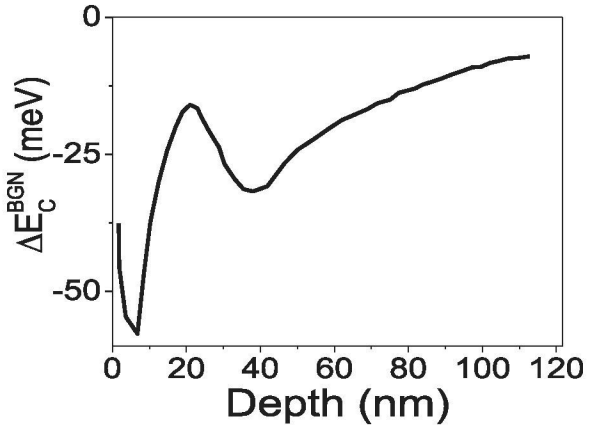

FIG. 9. Conduction band gap narrowing corresponding to the $10^{14}\,cm^{-2}$ implantation dose.

The tunneling rate for a barrier of energy Φ_B and thickness W_B is proportional to $\exp - [(2\sqrt{2m_{eff}\Phi_B})W_B/h]$, where h is the Plank's constant and m_{eff} is the free effective electron mass. On the other hand, thermal emission rate from a trap with an energy E_T is proportional to $\exp - [E_T/kT]$. In our case, the energy barrier is essentially equal to the trap energy ($E_T = \Phi_B$). Therefore, tunneling will be dominant at temperatures lower than $T_{eq} = h\sqrt{E_T}/(2KW_B\sqrt{2m_{eff}})$. In the case of silicon, assuming $m_{eff} = 0.26m_0$, (where m_0 is the free electron mass), we obtain

$$T_{eq} = 276\sqrt{E_T(\text{meV})}/W_B(\text{nm}). \quad (3)$$

For instance, for a trap with energy of 100 meV and located at a distance of 27.6 nm inside the transition region, $T_{eq} = 100$ K. At lower temperatures, tunneling dominates. These numbers are in the range of those obtained in our work, so confirming the validity of our assumptions.

As for the levels detected by TAS, the voltage bias dependency of the energy can be explained with the approach sketched in Fig. 8. The admittance peak that appears at higher temperatures in Figs. 3 and 4 is due to the Ti deep level existing at the n-type region. As it is well known, deep level conductance signal occurs at the point of the space charge region, λ, where the deep level crosses the Fermi level, E_F. As reverse bias increases, the space charge region becomes thicker and, then, λ reaches deeper positions in the n-type substrate, where the deep level concentration decays in an exponential way. The space charge region width can be easily calculated from experimental capacitance-voltage measurements. In our samples, capacitance values range from 2 nF at zero bias to 500 pF at 8 V corresponding to space charge region widths in the range of 0.5–2 μm. As the point λ is very close to the space charge region border,[25] we can ensure that the discrete energy level is measured in the n-type region, farther away from the transition region. That is why the deep level is only detected at high reverse voltages. As for the quasi-continuum levels, only the states with energy equal to the Fermi level contribute to the admittance signal. When varying the temperature, a maximum on the conductance and an inflection point on the capacitance appear at temperatures where the emission rate of these

levels is around the small signal frequency (Eqs. (1) and (2)). As voltage bias increases, the Fermi level crosses at deeper levels so explaining the dependencies plotted in Figure 7. Additionally, because deeper levels have lower emission rates, the conduction maxima appear at higher temperatures as reverse voltage increases (see Figs. 3–5).

Focusing now in the capture cross section values, we can see in the semi-logarithmic plot versus bias values of Fig. 7(b) that the distribution of the values perfectly matches with the distribution shown in Fig. 7(a). That means that if we plot all the capture cross section versus the activation energy values, we obtain a dependence that fits to a semi-logarithmic relationship. This relationship is called the Meyer-Neldel rule.[33,34] Found at the first time in 1937, this relation establishes that in magnitudes which follow an Arrhenius law there is dependence between the pre-exponential factor and the activation energy.

The emission rate of a deep level is given by[35]

$$e^t(T) = \sigma_T v_{th} N_C \cdot e^{-E_T/kT}. \tag{4}$$

Here, v_{th} is the carrier thermal velocity which is proportional to $T^{1/2}$ and N_c is the conduction band state density which is proportional to $T^{3/2}$. Equation (4) can be now rewritten as

$$e^t(T)/T^2 = \gamma\sigma_T \cdot e^{-E_T/kT}, \tag{5}$$

where γ includes the terms of v_{th} and N_c that do not depend on temperature. In this case, the dependence predicted by the Meyer-Neldel rule between the pre-exponential factor and the activation energy is given by

$$\sigma_T = \sigma_{TT} \cdot e^{E_T/kT_{mn}}, \tag{6}$$

where T_{mn} is called the Meyer-Neldel temperature and kT_{mn} is the Meyer-Neldel energy.

Figure 10 (red line) gives a consistent evidence of this relationship, leading the following values: $kT_{mn} = 15.19$ meV, and $T_{mn} = 17.6$ K.[21] It is very important to remark here that all the experimentally measured energy levels follow this law. That means that the relationship between capture cross section and energy follows a universal law, regardless the physical origin or the nature of the defect.

There are several references reporting this behavior for different magnitudes in semiconductor devices: forward current in diodes,[36] reverse current in solar cells,[37] and dark current in CCD devices.[38] In a previous work,[39] we studied silicon substrates for photovoltaic applications with different crystalline quality. Deep levels with energy values associated to iron atoms were observed. The iron atoms contaminated the samples during the fabrication process. Using the experimental results of that work, we can see that the capture cross section of the deep levels existing in those samples also follows the Meyer-Neldel rule. In fact, the capture cross section versus activation energy has been plotted in Figure 10 for samples fabricated on multicrystalline substrates (green points). The Meyer-Neldel energy value ($kT_{mn} = 13.65$ meV) is very close to the one obtained for samples implanted with titanium. The difference in the quality of the fit could be due to the difference between the very nature of the energy levels: very high implantation doses versus regular contamination concentrations.

Because of the variety of situations where this rule appears, it is very likely that this behavior cannot be associated to a particular process, but to a more fundamental phenomenon like multi excitation entropy theory.[40] Therefore, the Meyer-Neldel rule takes place in disordered systems where processes affected by this rule involve multiple excitations.[41] For instance, the emission or capture of a carrier in a deep level is a process in this way.[42] However, according to Yelon,[43] the idea of assume T_{mn} as a measure of disorder, increasing with T_{mn}, does not appear to be correct at all. Instead, virtually all solid-state phenomena give values of kT_{mn} that can be associated to the typical phonon energies. This fact matches with the similarity of kT_{mn} values obtained in both kinds of samples based in the same substrate material (silicon).

Finally, to facilitate the visualization of the dependence between the activation energy and the capture cross section obtained in this study, we include the Figure 11. This figure is a three-dimensional plot of Equation (5). For each energy

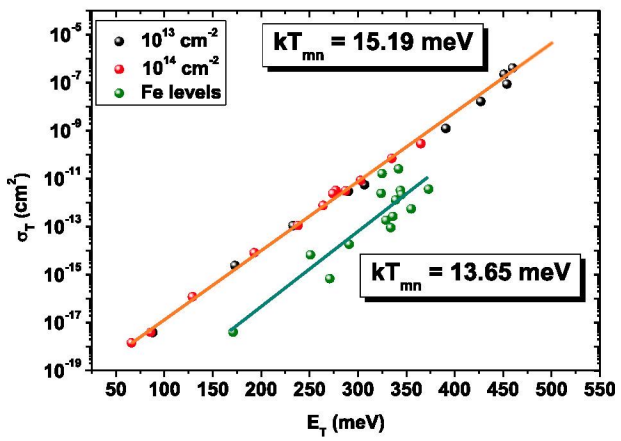

FIG. 10. Capture cross section vs. activation energy at different bias values in both silicon samples implanted with Ti (red line) and silicon samples contaminated with Fe (green line).

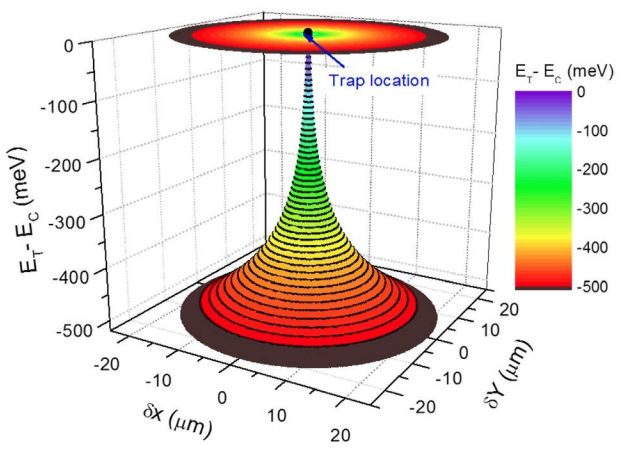

FIG. 11. Three dimensional plot and contour map showing the traps capture cross section as a function of the trap energy level.

value, we draw a circle with an area equal to the capture cross section, σ_T, that is, with a radius given by

$$r_T = \sqrt{(\delta_x^2 + \delta_y^2)} = \sqrt{\frac{\sigma_T}{\pi}}. \quad (7)$$

Only electrons located inside this area are captured by the trap. The color map on the top is the XY projection of the 3D plot and means how close a free electron must be from an empty trap location to be captured by it. Deeper traps are able to trap electrons located farther away from the trap according to an exponential law (Eq. (6)).

V. CONCLUSIONS

The study in depth of the energy levels present on silicon substrates supersaturated with Ti reported a complex configuration. A model is proposed consisting of different energy level configurations depending on the Ti concentration: a continuum-energy intermediate band is formed when Ti concentration is over the Mott limit, quasi-continuum levels for very high concentrations but below the Mott limit, and single deep level configuration for low Ti concentration. Conductance transients were obtained at low temperature which increase at the beginning and decay up to a frequency dependent stationary value for long times. This behavior is due to the band-gap narrowing induced at the highly titanium doped regions. The band-gap narrowing creates an energy barrier for electrons on the conduction band with values of several tens of meV. At low temperatures, forward current consists of electrons that pass this barrier by tunneling. This is a time consuming mechanism which is responsible for the initial transient and the stationary value of the conductance measurements.

The relationship among the activation energy and capture cross section values of these energy levels follows the Meyer-Neldel rule, which commonly appears on processes involving multiple excitations, like carrier capture and emission processes in deep levels, in high disordered systems. The results show a linear dependence among these two magnitudes as the Meyer-Neldel rule establishes. The value obtained for the characteristic energy of this phenomenon is: $kT_{mn} = 15.19$ meV. From the experimental data of a different study focused on silicon substrates contaminated with Fe, we obtain a similar value: $kT_{mn} = 13.65$ meV. That means that the energy value obtained could be associated to the characteristic energy of the phonons involved in the carrier emission and capture processes in the deep levels detected.

ACKNOWLEDGMENTS

The study has been supported by the Spanish TEC2014 under Grant No. 52152-C3-3-R, TEC2013-41730-R funded by the Ministerio de Economía y Competitividad, and the P2013/MAE-2780 funded by the Comunidad de Madrid. Research of E. Pérez was supported by a University of Valladolid FPI Grant. J. Olea acknowledges financial support from the MICINN within the program Juan de la Cierva (JCI-2011-10402), under which this research was undertaken. Research by E. García-Hemme was also supported by a PICATA predoctoral fellowship of the Moncloa Campus of International Excellence (UCM-UPM).

[1]A. Luque and A. Martí, Phys. Rev. Lett. **78**, 5014 (1997).
[2]G. González-Díaz, J. Olea, I. Mártil, D. Pastor, A. Martí, E. Antolín, and A. Luque, Sol. Energy Mater. Sol. Cells **93**, 1668 (2009).
[3]A. Luque and A. Martí, *Handbook of Photovoltaic Science and Engineering*, 2nd ed. (John Wiley & Sons, New Jersey, 2011), p. 130.
[4]A. Martí and G. L. Araújo, Sol. Energy Mater. Sol. Cells **43**, 203 (1996).
[5]E. García-Hemme, R. García-Hernansanz, J. Olea, D. Pastor, A. del Prado, I. Mártil, and G. González-Díaz, Appl. Phys. Lett. **103**, 032101 (2013).
[6]J. P. Mailoa, A. J. Akey, C. B. Simmons, D. Hutchinson, J. Mathews, J. T. Sullivan, D. Recht, M. T. Winkler, J. S. Williams, J. M. Warrender, P. D. Persans, M. J. Aziz, and T. Buonassisi, Nat. Commun. **5**, 3011 (2014).
[7]P. Lam, J. Wu, M. Tang, Q. Jiang, S. Hatch, R. Beanland, J. Wilson, R. Allison, and H. Liu, Sol. Energy Mater. Sol. Cells **126**, 83 (2014).
[8]Y. J. Kuang, K. M. Yu, R. Kudrawiec, A. V. Luce, M. Ting, W. Walukiewicz, and C. W. Tu, Appl. Phys. Lett. **102**, 112105 (2013).
[9]T. Tanaka, M. Miyabara, Y. Nagao, K. Saito, Q. Guo, M. Nishio, K. M. Yu, and W. Walukiewicz, Appl. Phys. Lett. **102**, 052111 (2013).
[10]W. Shan, W. Walukiewicz, J. W. Ager III, E. E. Haller, J. F. Geisz, D. J. Friedman, J. M. Olson, and S. R. Kurtz, Phys. Rev. Lett. **82**, 1221 (1999).
[11]C. Malerba, C. L. Azanza Ricardo, M. D'Incau, F. Biccari, P. Scardi, and A. Mittiga, Sol. Energy Mater. Sol. Cells **105**, 192 (2012).
[12]J. Olea, M. Toledano-Luque, I. Mártil, and G. González-Díaz, Springer Ser. Opt. Sci. **165**, 321 (2012).
[13]J. Olea, M. Toledano-Luque, D. Pastor, G. González-Díaz, and I. Mártil, J. Appl. Phys. **104**, 016105 (2008).
[14]D. Mathiot and S. Hocine, J. Appl. Phys. **66**, 5862 (1989).
[15]L. Tilly, H. G. Grimmeiss, H. Pettersson, K. Schmalz, K. Tittelbach, and H. Kerkow, Phys. Rev. B **43**, 9171 (1991).
[16]J-W. Chen, A. G. Milnes, and A. Rohatgi, Solid State Electron. **22**, 801 (1979).
[17]J. R. Morante, J. E. Carceller, and P. Cartujo, Solid State Electron. **26**, 1 (1983).
[18]W. Shockley and W. T. Read, Jr., Phys. Rev. **87**, 835 (1952).
[19]R. N. Hall, Phys. Rev. **87**, 387 (1952).
[20]A. Luque, A. Martí, E. Antolín, and C. Tablero, Physica B **382**, 320 (2006).
[21]E. Pérez, H. Castán, H. García, S. Dueñas, L. Bailón, D. Montero, R. García-Hernansanz, E. García-Hemme, J. Olea, and G. González-Díaz, Appl. Phys. Lett. **106**, 022105 (2015).
[22]H. Castán, E. Pérez, H. García, S. Dueñas, L. Bailón, J. Olea, D. Pastor, E. García-Hemme, M. Irigoyen, and G. González-Díaz, J. Appl. Phys. **113**, 024104 (2013).
[23]J. Olea, M. Toledano-Luque, D. Pastor, E. San-Andrés, I. Mártil, and G. González-Díaz, J. Appl. Phys. **107**, 103524 (2010).
[24]G. I. Roberts and C. R. Crowell, J. Appl. Phys. **41**, 1767 (1970).
[25]J. Barbolla, S. Dueñas, and L. Bailón, Solid-State Electron. **35**(3), 285 (1992).
[26]H. Bayhan and A. S. Kavasoglu, Turk. J. Phys. **27**, 529 (2003).
[27]S. Dueñas, R. Peláez, H. Castán, R. Pinacho, L. Quintanilla, and J. Barbolla, Appl. Phys. Lett. **71**, 826 (1997).
[28]H. Castán, S. Dueñas, J. Barbolla, E. Redondo, N. Blanco, I. Mártil, and G. González-Díaz, Microelectron. Reliab. **40**, 845 (2000).
[29]U. Lindefelt, J. Appl. Phys. **84**(5), 2628 (1998).
[30]J. Olea, G. González-Díaz, D. Pastor, I. Mártil, A. Martí, E. Antolín, and A. Luque, J. Appl. Phys. **109**, 063718 (2011).
[31]S. C. Jain and D. J. Roulston, Solid State Electron. **34**(5), 453 (1991).
[32]V. Palankovski, G. Kaiblinger-Grujin, and S. Selberherr, Mater. Sci. Eng. **B66**, 46 (1999).
[33]W. Meyer and H. Neldel, Z. Tech. Phys. **18**, 518 (1937).
[34]Y. F. Chen and S. F. Huang, Phys. Rev. B **44**, 13775 (1991).
[35]D. K. Schroder, *Semiconductor Material and Device Characterization*, 2nd ed. (John Wiley & Sons, New Jersey, USA, 1998).
[36]R. Widenhorn, M. Fitzgibbons, and E. Bodegom, J. Appl. Phys. **96**, 7379 (2004).

[37]T. J. Coutts and N. M. Pearsall, Appl. Phys. Lett. **44**, 134 (1984).
[38]R. Widenhorn, L. Mündermann, A. Rest, and E. Bodegom, J. Appl. Phys. **89**, 8179 (2001).
[39]E. Pérez, H. García, H. Castán, and S. Dueñas, Semicond. Sci. Technol. **30**, 035011 (2015).
[40]A. Yelon, B. Movoghar, and R. S. Crandall, Rep. Prog. Phys. **69**, 1145 (2006).
[41]A. Yelon, B. Movoghar, and H. M. Branz, Phys. Rev. B **46**, 12244 (1992).
[42]D. V. Lang and C. H. Henry, Phys. Rev. Lett. **35**, 1525 (1975).
[43]A. Yelon, Monatsh. Chem. **144**, 91 (2013).